Supplementary Information: Demonstrating experimentally the encoding and dynamics of an error-correctable logical qubit on a hyperfine-coupled nuclear spin qudit

Sumin Lim, Mikhail Vaganov, Junjie Liu, and Arzhang Ardavan
CAESR, Department of Physics, University of Oxford,
The Clarendon Laboratory, Parks Road, Oxford OX1 3PU, UK

I. OPERATIONS ENCODING AND DECODING THE LOGICAL QUBIT

In this section we present the detailed operations by which the qubit state in Eqn. 2 of the main manuscript is rotated onto the the logical qubit state in Eqn. 3, and the decoding operation rotating the state in Eqn. 6 to the state in Eqn. 7. In quantum spin systems, controlled rotations between states with $\Delta m_S = \pm 1$ or $\Delta m_I = \pm 1$ may be achieved using magnetic resonance pulses; in specific circumstances [1, 2] $\Delta m_S = \pm 2$ or $\Delta m_I = \pm 2$ transitions are also available. The protocol described here depends on each of these transitions being spectrally addressable, as is the case, for example, in the Mn:ZnO system.

In a two-state system, the basic operation is a rotation

$$R_{|-\frac{1}{2}\rangle\leftrightarrow|+\frac{1}{2}\rangle,\theta} = \exp\left(-\frac{\mathrm{i}\theta\sigma_y}{2}\right) = \begin{pmatrix} \cos\left(\frac{\theta}{2}\right) & -\sin\left(\frac{\theta}{2}\right) \\ \sin\left(\frac{\theta}{2}\right) & \cos\left(\frac{\theta}{2}\right) \end{pmatrix} \tag{S1}$$

where the axis of the rotation (which, here, is the y-axis in the rotating frame) is chosen by adjusting the phase of the magnetic resonance pulse, and the angle of the rotation, θ, is controlled by adjusting the duration or the amplitude of the pulse.

A. Encoding and decoding within the $m_S = -\frac{1}{2}$ subspace

At the heart of the protocol is a unitary transformation within the $m_S = -\frac{1}{2}$ subspace,

$$\begin{aligned} U_{\text{enc}} = &|0_L\rangle\left\langle -\frac{1}{2}, -\frac{1}{2}\right| \\ &+ |1_L\rangle\left\langle -\frac{1}{2}, +\frac{1}{2}\right| \\ &+ |I_z 0_L\rangle\left\langle -\frac{1}{2}, -\frac{3}{2}\right| \\ &+ |I_z 1_L\rangle\left\langle -\frac{1}{2}, +\frac{3}{2}\right| \end{aligned} \tag{S2}$$

where $|m_S, m_I\rangle \equiv |m_S\rangle \otimes |m_I\rangle$, $|0_L\rangle$ and $|1_L\rangle$ are defined in Eqn. 4 of the main manuscript, and

$$\begin{aligned} |I_z 0_L\rangle &= \frac{2}{\sqrt{3}}\hat{I}_z|0_L\rangle \\ |I_z 1_L\rangle &= \frac{2}{\sqrt{3}}\hat{I}_z|1_L\rangle \end{aligned} \tag{S3}$$

with factors of $2/\sqrt{3}$ included for normalisation. U_{enc} encodes a nuclear spin qubit

$$\alpha\left|-\frac{1}{2},-\frac{1}{2}\right\rangle+\beta\left|-\frac{1}{2},+\frac{1}{2}\right\rangle \tag{S4}$$

to the state $|\psi_L\rangle$ given in Eqn. 3 of the main manuscript.

Under the action of the perturbation, $|0_L\rangle$ and $|1_L\rangle$ are mixed with $|I_z 0_L\rangle$ and $|I_z 1_L\rangle$ respectively.

The inverse transformation, $U_{\mathrm{enc}}^{\dagger}$, decodes from the protected basis so that the uncorrupted component is restored to the state in Eqn. S4, and the error component arrives on the superposition

$$\epsilon\left(\alpha\left|-\frac{1}{2},-\frac{3}{2}\right\rangle+\beta\left|-\frac{1}{2},+\frac{3}{2}\right\rangle\right) \tag{S5}$$

where, comparing with Eqns. 6 and 7 of the main manuscript, $\epsilon=-\mathrm{i}\theta$.

The practical implementation of U_{enc} depends on the operations that are available in the specific physical system on which the protocol is to be implemented. For a system in which $\Delta m_I=\pm 1,\pm 2$ transitions are available, an efficient operation yielding U_{enc} is provided by the sequence of pulses represented by operators (to be read from right to left)

$$R_{\left|-\frac{1}{2}\right\rangle\leftrightarrow\left|+\frac{3}{2}\right\rangle,\frac{\pi}{3}}\cdot R_{\left|-\frac{3}{2}\right\rangle\leftrightarrow\left|+\frac{1}{2}\right\rangle,\frac{5\pi}{3}}\cdot R_{\left|-\frac{1}{2}\right\rangle\leftrightarrow\left|+\frac{1}{2}\right\rangle,-\pi}\,. \tag{S6}$$

The decoding pulse sequence implementing $U_{\mathrm{enc}}^{\dagger}$ is generated by reversing the sequence of pulses and replacing θ with $-\theta$ for each.

In physical systems for which only $\Delta m_I=\pm 1$ transitions are available, alternative equivalently functional encodings within this space can be identified.

B. Swapping between electron and nuclear spin states

The encoding between main manuscript Eqns. 2 and 3 requires a step before the operation described in Section I A, transferring the electron qubit state in Eqn. 2 of the main manuscript onto the nuclear qubit Eqn. S4. This operation can be achieved using a sequence of one nuclear π pulse and one electron π pulse [3],

$$R_{\left|-\frac{1}{2},+\frac{1}{2}\right\rangle\leftrightarrow\left|+\frac{1}{2},+\frac{1}{2}\right\rangle,\pi}\cdot R_{\left|+\frac{1}{2},-\frac{1}{2}\right\rangle\leftrightarrow\left|+\frac{1}{2},+\frac{1}{2}\right\rangle,-\pi}\,. \tag{S7}$$

Following the decoding transformation described in Section I A, the uncorrupted component is already in the superposition given by the first term in main manuscript Eqn. 7.

The final decoding step is to transfer the corrupted component from the $\left|-\frac{1}{2},-\frac{3}{2}\right\rangle, \left|-\frac{1}{2},+\frac{3}{2}\right\rangle$ superposition to the $\left|+\frac{1}{2},-\frac{1}{2}\right\rangle, \left|+\frac{1}{2},+\frac{1}{2}\right\rangle$ superposition. This is achieved through a pair of electron π pulses followed by a pair of nuclear π pulses,

$$R_{|+\frac{1}{2},+\frac{1}{2}\rangle\leftrightarrow|+\frac{1}{2},+\frac{3}{2}\rangle,\pi} \cdot R_{\left|+\frac{1}{2},-\frac{3}{2}\right\rangle\leftrightarrow|+\frac{1}{2},-\frac{1}{2}\rangle,-\pi} \cdot R_{\left|-\frac{1}{2},+\frac{3}{2}\right\rangle\leftrightarrow|+\frac{1}{2},+\frac{3}{2}\rangle,-\pi} \cdot R_{\left|-\frac{1}{2},-\frac{3}{2}\right\rangle\leftrightarrow|+\frac{1}{2},-\frac{3}{2}\rangle,-\pi} \cdot \tag{S8}$$

C. Our experimental encoding stage

Owing to the lack of projective measurement in our apparatus, there is no value in our experiment implementing the full decoding described here. Instead we use a simpler but equivalent encoding, and we explore the dynamics of the encoded state by detecting various coherences as described in the main manuscript and in Section V.

II. LOW-TEMPERATURE RELAXATION FOR THE ELECTRON SPINS

The spin-lattice relaxation time ($T_{1\mathrm{e}}$) for the electron is measured employing the standard inversion recovery sequence [$\pi - T - \pi/2 - \tau - \pi -$ echo], recording the echo intensity vs. T. The phase coherence time ($T_{2\mathrm{e}}$) for the electron spins is measured by the standard Hahn-echo sequence [$\pi/2 - T - \pi - T -$echo] and fitting the echo intensity vs. the coherence storage time $2T$. The results are shown in Fig. S1. The measurements are performed at 30 K with the static magnetic field of 0.3433 T, which corresponds to the resonance condition for the ESR transition between the $m_S = \pm 1/2$ states with $m_I = -1/2$. Both data are well described by single exponential functions, yielding $T_{1\mathrm{e}} = 1.3 \pm 0.045$ ms and $T_{2\mathrm{e}} = 80 \pm 4.05\,\mu$s.

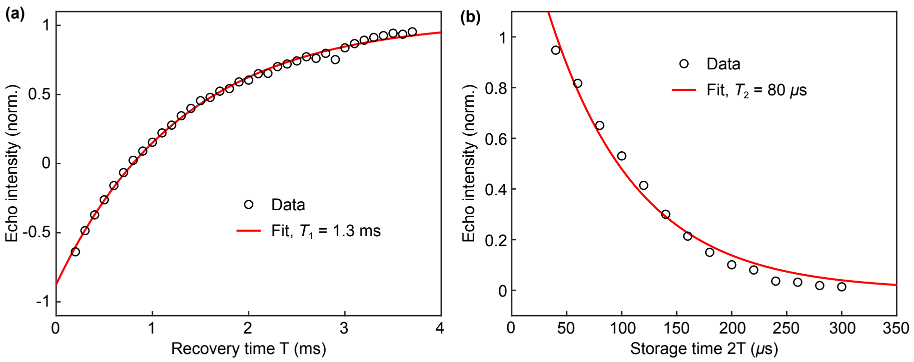

FIG. S1. The measurement of **(a)** the spin-lattice relaxation time $T_{1\mathrm{e}}$ and **(b)** the phase coherence time $T_{2\mathrm{e}}$.

III. ELECTRON-NUCLEAR DOUBLE RESONANCE (ENDOR) AND COHERENCE TRANSFERS OF QUANTUM INFORMATION BETWEEN ELECTRON AND NUCLEAR SPINS

Direct measurement of the Mn nuclear spins is only possible at very high doping levels which significantly compromises the coherence time of the electron spins. Therefore, we apply electron-nuclear double resonance techniques to control both the electron and nuclear spins, and measure the nuclear spins by means of electron spin echoes. The protocol for encoding the logical qubit utilises the nuclear spin subspace $m_I = \pm 1/2$ and $\pm 3/2$ (all with $m_S = -1/2$). Hence, it is essential that we are able to generate superpositions between any nuclear spin states in this subspace using RF control pulses. This requires access to three nuclear spin transitions, $f_1 : |-1/2\rangle \otimes |-1/2\rangle \leftrightarrow |-1/2\rangle \otimes |+1/2\rangle$, $f_2 : |-1/2\rangle \otimes |-1/2\rangle \leftrightarrow |-1/2\rangle \otimes |-3/2\rangle$ and $f_3 : |-1/2\rangle \otimes |+1/2\rangle \leftrightarrow |-1/2\rangle \otimes |+3/2\rangle$. (All states are represented using the $|m_S\rangle \otimes |m_I\rangle$ notation). In the experiment, the static magnetic field B_0 is fixed at 0.3443 T, which corresponds to the resonance field of the $|-1/2\rangle \otimes |-1/2\rangle \leftrightarrow |+1/2\rangle \otimes |-1/2\rangle$ ESR transition. This combination of MW frequency and magnetic field allows us to access f_1 and f_2 nuclear spin transitions directly using the standard Davies ENDOR sequence [Fig. S2(a)]. The result is shown in the red curve in Fig. S2(d). When sweeping the frequency of the RF $\pi(f)$-pulse, two resonance peaks are observed, corresponding to the two allowed nuclear spin transitions involving the $|-1/2\rangle \otimes |-1/2\rangle$ state.

Accessing the $f_3 : |-1/2\rangle \otimes |+1/2\rangle \leftrightarrow |-1/2\rangle \otimes |+3/2\rangle$ transition is more challenging. In order to measure the nuclear transition frequency f_3, we first introduce the coherence transfer scheme used in this work. This scheme, together with its variations, allow us to transfer electron coherence to the nuclear spins and detect it in a highly diluted sample. Fig. S2(b) shows the pulse sequence used to transfer, store and measure the coherence between $m_I = \pm 1/2$ states. A coherence is first generated by the initial MW $\pi/2$ pulse, placing the electron spins into the superposition of $|-1/2\rangle \otimes |-1/2\rangle$ and $|+1/2\rangle \otimes |-1/2\rangle$ states. The following MW π pulse refocusses the electron spins to mitigate the free induction decay due to inhomogeneities, allowing the coherence to be transferred to the nuclear spins by the following RF and MW π pulses indicated by the dashed box. The coherence generated by the first MW $\pi/2$ pulse is now completely stored in the nuclear spin, between the superposition of the $|-1/2\rangle \otimes |-1/2\rangle$ and $|-1/2\rangle \otimes |+1/2\rangle$ states. This quantum coherence may be

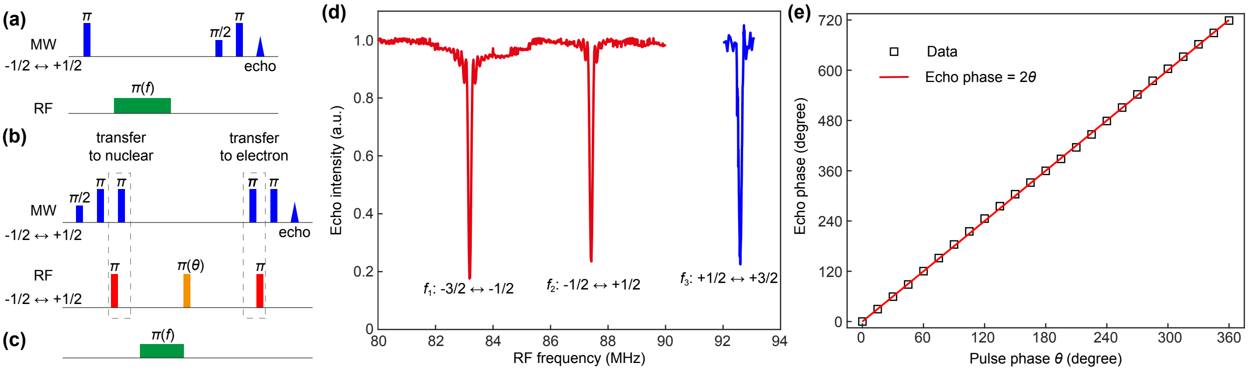

FIG. S2. **(a)** the standard Davies ENDOR sequence used to measure the allowed ($\delta m_I = \pm 1$) nuclear spin resonance from the $|-1/2\rangle \otimes |-1/2\rangle$ state. The echo intensity is recorded while varying the frequency of the RF pulse $\pi(f)$ to match the resonance conditions. **(b)** the pulse sequence that implements the transfer of quantum coherence between the electron and nuclear spins. **(c)** an additional RF pulse $\pi(f)$ is inserted to the coherence transfer sequence in **(b)**, allowing the detection of the $|-1/2\rangle \otimes |+1/2\rangle \leftrightarrow |-1/2\rangle \otimes |+3/2\rangle$ resonance frequency by tuning the frequency of $\pi(f)$. **(d)** the echo intensity as a function of the frequency of the pulse $\pi(f)$. The red curve is measured using the sequence in **(a)** and the blue trace is recored using the sequence described in **(b)** and **(c)**. **(e)** the phase of the final electron spin echo as a function of the phase of the refocusing pulse $\pi(\theta)$ in **(b)**, confirming the measured coherence is stored in the nuclear spins.

stored for an extended period (of the time scale of the nuclear $T_{2\mathrm{n}}$). A RF refocussing pulse, $\pi(\theta)$ of phase of θ is applied at the halfway point of the storage time to remove the effects of inhomogeneities associated with the nuclear spin, allowing the remaining coherence to be transferred back to the electron spins and measured using the electron spin echo.

A four-step phase cycling of the initial MW $\pi/2$ and the RF π refocussing pulses (Table. I) is implemented to remove undesired echo contributions, including the stimulated electron spin echo (which decays on the timescale of T_{1e}), electron echo/free induction decay due to the last two MW π pulses, and the detector DC offset, ensuring the measured echo signal is purely due to the coherence transfer via the nuclear spins. This is further verified by varying the phase of the RF refocusing pulse $\pi(\theta)$. Only the coherence stored in the nuclear spins is expected to gain an additional phase factor of 2θ, which can be measured in the final electron spin echo, whereas all other undesired echo contributions are insensitive to θ. The data in Fig. S2(e) match with the 2θ expectation perfectly, confirming all the detect signals are transferred via the electron-nuclear-electron pathway.

TABLE I. The phase cycling sequence and the signal for the coherence transfer scheme.

Step number	MW $\pi/2$ pulse	RF refocusing pulse	Signal
1	$+x$	$+x$	$+$
2	$-x$	$+x$	$-$
3	$+x$	$+y$	$-$
4	$-x$	$+y$	$+$

Finally, we present the measurement of the $|-1/2\rangle \otimes |+1/2\rangle \leftrightarrow |-1/2\rangle \otimes |+3/2\rangle$ transition frequency using a modified ENDOR sequence. The sequence is largely identical to the coherence transfer scheme [Fig. S2(b)] with an additional RF pulse $\pi(f)$ applied between the first two RF $|-1/2\rangle \otimes |-1/2\rangle \leftrightarrow |-1/2\rangle \otimes |+1/2\rangle$ pulses [Fig. S2(c)]. When the frequency of the $\pi(f)$ pulse matches that for the $|-1/2\rangle \otimes |+1/2\rangle \leftrightarrow |-1/2\rangle \otimes |+3/2\rangle$ nuclear transition, the nuclear spin coherence is transferred and stored between the superposition of the $|-1/2\rangle \otimes |-1/2\rangle$ and $|-1/2\rangle \otimes |+3/2\rangle$ states instead. Under this circumstance, the coherence cannot be transferred back to the electron spins by the same pulse sequence, leading to a reduction of the electron spin echo, as shown by the blue curve in Fig. S2(d).

In summary, we successfully identified the three RF transitions: $f_1 = 83.2$ MHz for $|-1/2\rangle \otimes |-3/2\rangle \leftrightarrow |-1/2\rangle \otimes |-1/2\rangle$, $f_2 = 87.4$ MHz for $|-1/2\rangle \otimes |-1/2\rangle \leftrightarrow |-1/2\rangle \otimes |+1/2\rangle$ and $f_3 = 92.6$ MHz for $|-1/2\rangle \otimes |+1/2\rangle \leftrightarrow |-1/2\rangle \otimes |+3/2\rangle$. Importantly, all three transitions are non-degenerate owing to the second order hyperfine coupling shifts, allowing selective access to any desired nuclear spin states for the implementation of the fault-tolerant encoding algorithm.

IV. TIME-DEPENDENCE OF NUCLEAR COHERENCES

As described in Section II, the sequence in Fig. S3(a) generates an electronic coherence on the $m_S = -1/2, +1/2$ transition within the $m_I = -1/2$ subspace, and transfers it to a nuclear coherence on the $m_I = -1/2, +1/2$ transition within the $m_S = -1/2$ subspace, and finally restores it to the electronic state for read out via an ESR echo. In here, we measure the time dependence of the nuclear coherence decay by varying nuclear-storage-time.

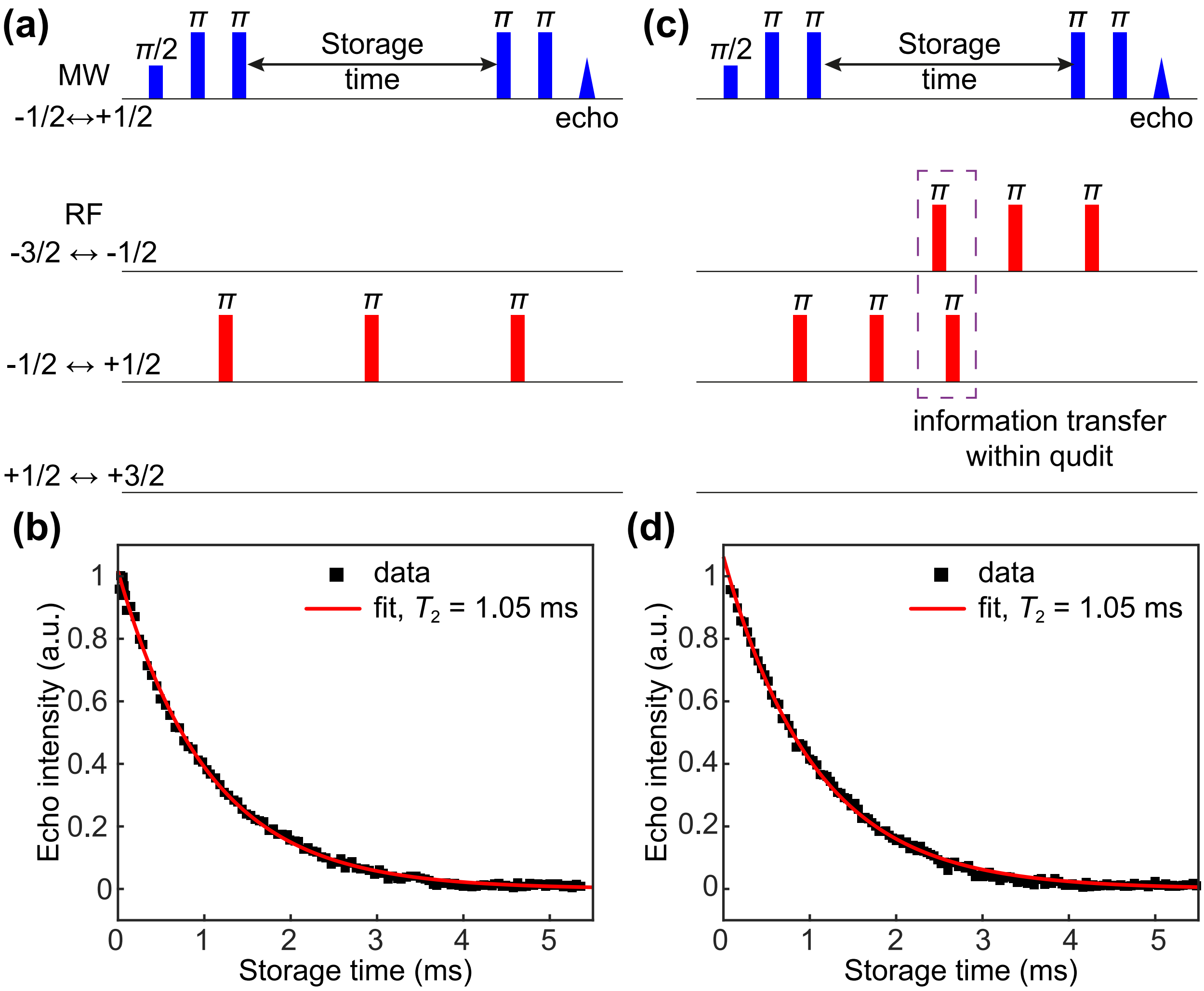

FIG. S3. Pulse sequences implementing coherence transfer between the electron qubit and coherences within the nuclear qudit. (a) An Electron-qubit is transferred to the nuclear $m_I = \pm 1/2$ coherence, stored for a time, and then transferred back to the electron qubit where it is read out through an electron spin echo. (b) By varying the storage time, we obtain $T_{2\mathrm{n}}$ from the echo decay. (c) Quantum information can be transferred between states within the qudit, in this case between the $m_I = \pm 1/2$ coherence and the $m_I = -3/2, m_I = -1/2$ coherence. By varying the storage time, we confirm (d) the same phase coherence time for each qudit transition.

Fig. S3(b) shows the recovered coherence amplitude as a function of the delay time, while the microwave pulse durations, the RF pulse durations, and microwave pulse intervals were kept fixed at 0.1 μs, 7 μs, and 8 μs, respectively. The exponential decay constant yields the phase coherence time $T_{2\mathrm{n}} = 1.050 \pm 0.004$ ms for the $m_I = -1/2, +1/2$ transition. This is close to the $T_{1\mathrm{e}}$ time for the $m_S = -1/2, +1/2$ electronic transition at this temperature, indicating that phase relaxation is dominated by electronic spin flips. It exceeds very significantly the electronic $T_{2\mathrm{e}}$ time of about 80 μs, demonstrating successful coherence transfer. The phase of the detected electronic echo is controlled by the phase of the nuclear coherence refocussing pulse with the expected dependence (Fig. S2(e)), further confirming the storage of the coherence in the nuclear states.

The next step is to demonstrate coherence transfer within the nuclear qudit. In Fig. S3(c) we present a pulse sequence designed to transfer an electron coherence to a nuclear coherence ($m_I = -1/2, +1/2$), to transfer this coherence within the qudit (to $m_I = -1/2, -3/2$), and finally to transfer back to the electronic qubit for Hahn echo readout. By analogy with the experiment in Fig. S3(b), measuring the dependence of the read-out echo on the storage time allows us to compare the phase coherence times for different nuclear qudit coherences. As shown in Fig. S3(d), we find that the $m_I = -1/2, -3/2$ coherence time (1.05 ± 0.007ms) matches what we found for $m_I = -1/2, +1/2$; this is exactly as we expect given that electronic $T_{1\mathrm{e}}$ processes are likely to be the dominant cause of the nuclear qudit dephasing at this temperature.

These coherence transfer experiments allow us to calibrate the microwave and RF pulses corresponding to the operations required to implement the encoded state (Eqns. 3 and 4 in main text), with details described in Section IV.

V. THE THERMAL STATE AND STATE EVOLUTION

In this Section, we discuss the initial thermal population and identify it as effectively a pseudo-pure state. We then explain step by step the state evolution through the experimental pulse sequence.

A. The thermal state

In Fig. S4 (a), we indicate the initial thermal population for the relevant spin energy levels. The ground state of the system, $m_S = -5/2, m_I = -5/2$ (not shown), which will be exclusively populated for temperatures such that $k_B T$ is much smaller than any of the energy scales in the Hamiltonian, main manuscript Eqn. 8. However, for a range of practical

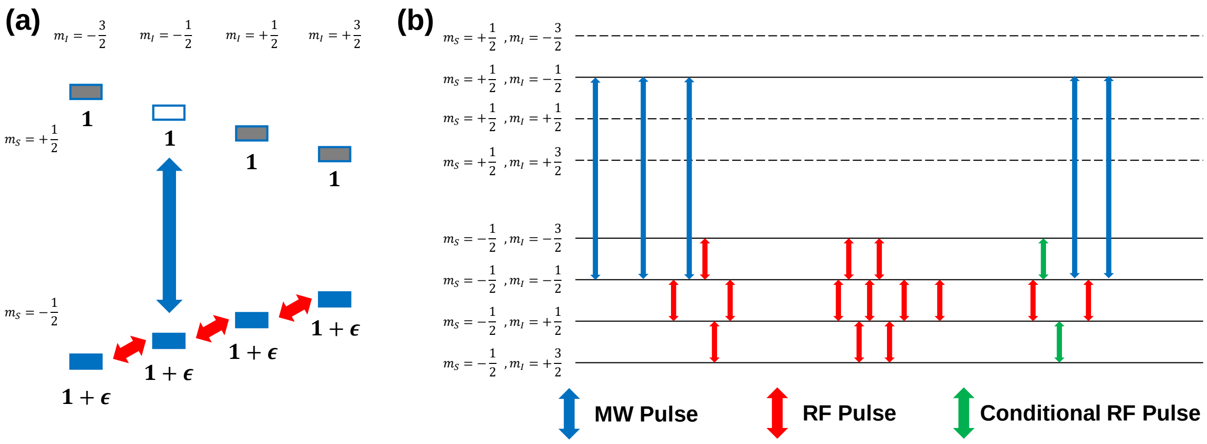

FIG. S4. (a) Initial thermal population of related spin states. (b) The detail (conditional) pulse sequence for each levels.

reasons we conduct the experiment at an elevated temperature, so we must consider the thermal equilibrium population distribution in our ensemble, which represents the starting state for each experimental shot.

The population of a state of energy E_i is proportional to the Boltzmann factor $e^{-\Delta E_i/k_B T}$. In our experiment, $k_B T \sim 620$ GHz , $E_{\text{Zeeman}} \sim 9.7$ GHz, and the nuclear transition frequencies ~ 0.08 GHz. This means that the initial population difference between the $m_S = \pm 1/2$ is orders of magnitude larger than population differences within each m_S manifold. Thus to a good approximation, the density matrix of the system is

$$\rho_{\text{Thermal}} = \begin{pmatrix} \frac{1}{5}+\frac{\delta}{4} & 0 & 0 & 0 & 0 \\ 0 & \frac{1}{5}+\frac{\delta}{4} & 0 & 0 & 0 \\ 0 & 0 & \frac{1}{5}+\frac{\delta}{4} & 0 & 0 \\ 0 & 0 & 0 & \frac{1}{5}+\frac{\delta}{4} & 0 \\ 0 & 0 & 0 & 0 & \frac{1}{5}-\delta \end{pmatrix} \tag{S9}$$

when written in the basis of states participating in the experiment,

$$\left\{ \left|-\frac{1}{2},-\frac{3}{2}\right\rangle, \left|-\frac{1}{2},-\frac{1}{2}\right\rangle, \left|-\frac{1}{2},+\frac{1}{2}\right\rangle, \left|-\frac{1}{2},+\frac{3}{2}\right\rangle, \left|+\frac{1}{2},-\frac{1}{2}\right\rangle \right\} \tag{S10}$$

with $|m_S, m_I\rangle \equiv |m_S\rangle \otimes |m_I\rangle$.

This can be decomposed into an identity component and a component proportional to a pure state,

$$\rho_{\text{Thermal}} = \left(\frac{1}{5} + \frac{\delta}{4}\right) \mathbf{I} - \frac{5\delta}{4} \begin{pmatrix} 0 & 0 & 0 & 0 & 0 \\ 0 & 0 & 0 & 0 & 0 \\ 0 & 0 & 0 & 0 & 0 \\ 0 & 0 & 0 & 0 & 0 \\ 0 & 0 & 0 & 0 & 1 \end{pmatrix} \tag{S11}$$

where $\mathbf{I}$ is the identity matrix and and $5\delta/4 \approx 0.015$. This kind of state is known as "pseudo-pure" [4] because the identity component does nothing under the unitary transformations in the experiment, and the remainder is "pure" with a reduced amplitude of $-5\delta/4$.

B. Encoding pulse sequence

In Fig.S4(b), we illustrate the experimental pulse sequence. This is the same as the sequence in Fig 2(a) of the main manuscript, but indicating explicitly between which levels each pulse is applied. In what follows, we track the evolution of the state as the sequence progresses, represented as a vector in the basis indicated in Eqn. S10.

We start with the pseudo-pure state presented in Section V A,

$$\begin{pmatrix} 0, & 0, & 0, & 0, & 1 \end{pmatrix} . \tag{S12}$$

All pulses are applied with a phase generating a rotation around the y-axis in the rotating frame. The first MW $\pi/2$ pulse generates a coherence

$$\begin{pmatrix} 0, & -\alpha, & 0, & 0, & \beta \end{pmatrix} \tag{S13}$$

with $\alpha = \beta = 1/\sqrt{2}$. The following MW π pulse refocuses the coherence. At the formation of the echo, the RF π pulse on $m_I = -1/2 \leftrightarrow m_I = +1/2$ followed by the MW π pulse transfer the coherence into the nuclear spin subspace,

$$\begin{pmatrix} 0, & \alpha, & -\beta, & 0, & 0, \end{pmatrix} \tag{S14}$$

The following three RF pulses, $\pi/3$ on $m_I = -3/2 \leftrightarrow m_I = -1/2$, $\pi/3$ on $m_I = +1/2 \leftrightarrow m_I = +3/2$, and RF $-\pi$ on $m_I = -1/2 \leftrightarrow m_I = +1/2$, transform the state to

$$-\begin{pmatrix} \frac{1}{2}\alpha, & \frac{\sqrt{3}}{2}\beta, & \frac{\sqrt{3}}{2}\alpha, & \frac{1}{2}\beta, & 0 \end{pmatrix} \tag{S15}$$

corresponding, within a global undetectable phase, to the logical qubit state $\alpha|0_L\rangle + \beta|1_L\rangle$.

C. Sequence for detection of $m_I = \pm 1/2$ and $m_I = \pm 3/2$ coherences

Following encoding, error application and refocusing, the state of the system is, in general,

$$\Big(\xi, \zeta, \eta, \lambda, 0\Big) \tag{S16}$$

As explained in the main manuscript, owing to the incomplete refocussing, the experimental objective is to detect the $m_I = \pm 1/2$ and $m_I = \pm 3/2$ coherences via electron spin echoes.

The RF π pulse on $m_I = -1/2 \leftrightarrow m_I = +1/2$ changes this state to

$$\Big(\xi, -\eta, \zeta, \lambda, 0\Big) \tag{S17}$$

Without the conditional (green) pulses, the coherence transfer sequence of a MW π pulse and an RF π pulse on $m_I = -1/2 \leftrightarrow m_I = +1/2$ yields the state

$$\Big(\xi, -\zeta, 0, \lambda, -\eta\Big)\ . \tag{S18}$$

The subsequent MW refocusing pulse generates an electron spin echo from the amplitudes $[\eta, -\zeta]$, yielding the quantities $I_{\pm\frac{1}{2}x}$ and $I_{\pm\frac{1}{2}y}$ in the main manuscript.

With the conditional (green) pulses, the state in Eqn. S17 is transformed to

$$\Big(\eta, \xi, -\lambda, \zeta, 0\Big) \tag{S19}$$

The coherence transfer sequence of a MW π pulse and an RF π pulse on $m_I = -1/2 \leftrightarrow m_I = +1/2$ then yields the state

$$\Big(\eta, \lambda, 0, \zeta, \xi\Big) \tag{S20}$$

The subsequent MW refocusing pulse generates an electron spin echo from the amplitudes $[-\xi, \lambda]$, yielding the quantities $I_{\pm\frac{3}{2}x}$ and $I_{\pm\frac{3}{2}y}$ in the main manuscript.

VI. PULSE FIDELITY ESTIMATIONS

The fidelity of the MW and RF pulses are calibrated to evaluate the errors introduced in the spin control sequences. The dominant error in our control pulses is the rotation angle error due to the B_1 inhomogeneity associated with the resonator/RF coil profiles. The error for the MW pulse is estimated by observing the Rabi oscillation of the electron spin echo over a number of periods by varying the power of the initial pulse in an electron Hahn echo sequence. The result is shown in Fig. S5(b).

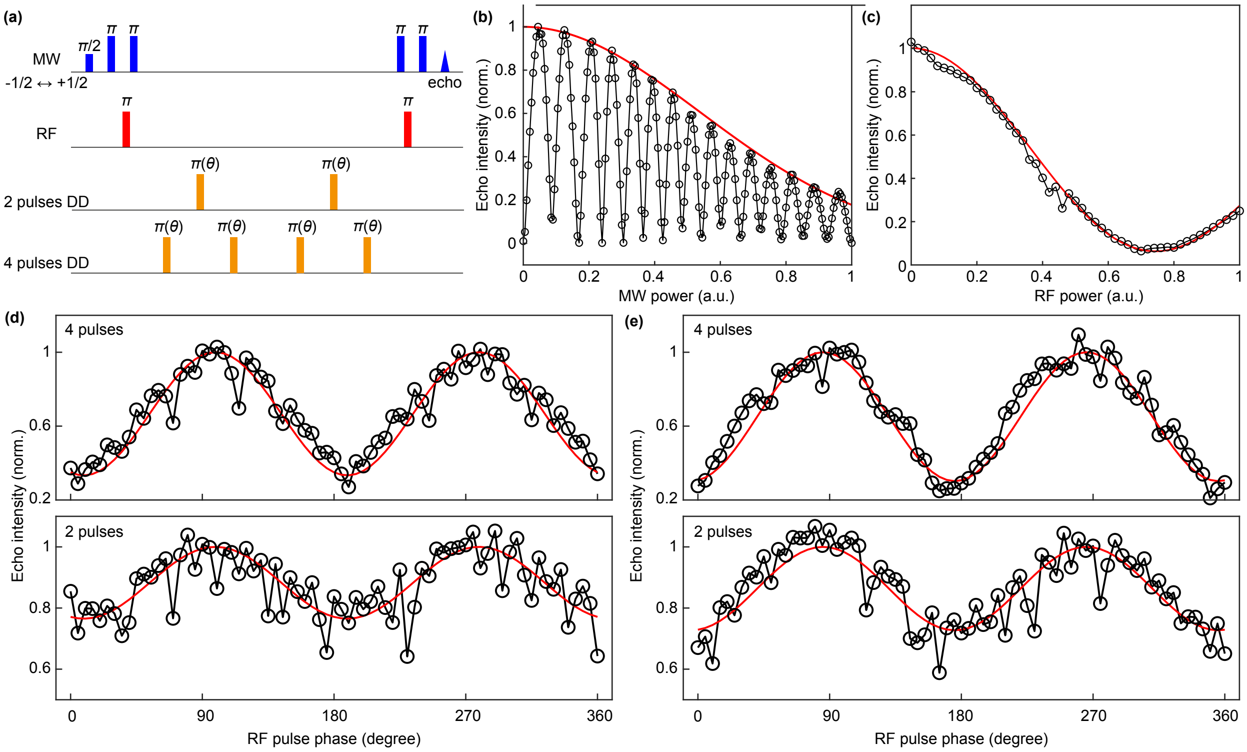

FIG. S5. **(a)** The pulse sequence employed to estimate the fidelity of the RF π pulses. All the red and orange pulses are RF pulses with the same frequency. We apply either the 2-pulses DD or the 4-pulse DD pulse train. The phase (θ) of the $\pi(\theta)$ pulses is swept in the experiment with the intensity of the final echo recorded as a function of θ. **(b)** the Rabi oscillation of the electron spin echo with varying the amplitude of the MW pulse. **(c)** The echo intensity of a standard Davis ENDOR sequence with varying the amplitude of the RF pulse. **(d)** and **(e)** show the intensity of the final echo as a function of θ measured using the pulse sequence in **(a)**. **(d)** and **(e)** are measured with the RF frequency of 83.2 MHz ($|-1/2\rangle \otimes |-3/2\rangle \leftrightarrow |-1/2\rangle \otimes |-3/2\rangle$) and 87.4 MHz ($|-1/2\rangle \otimes |-1/2\rangle \leftrightarrow |-1/2\rangle \otimes |+1/2\rangle$), respectively. The upper panels are the data measured with the 4-pulse DD train whereas the bottom panels are measured with the 2-pulse DD train.

From these data we can obtain a rotation angle error estimate following the procedure described in Reference [5]. The procedure models the B_1 inhomogeneity with a Gaussian distribution with standard deviation σ_{MW}. For a nutation sequence of n π-rotations (with $n\sigma_{MW} < 1$), the nth maximum is smaller than the first by a factor $\exp\left[-\sigma_{\mathrm{MW}}^2 n^2\right]$. Thus from the envelope of the nutation maxima, we can accurately extract the fidelity of a single π-rotation. The fidelity of our MW pulses estimated using this method is $99.5 \pm 0.1\%$.

We cannot use the same procedure for estimating the rotation angle error for our RF pulses, because, even at maximum power, we cannot obtain multiple π-rotations with a pulse of sufficient bandwidth; Fig. S5(c) shows the nuclear spin nutation over our available RF power range. In this situation, we use a variant of an alternative approach described in Reference [5]: comparing a Carr-Purcell echo train (which accumulates rotation angle errors from successive π pulses) with a Carr-Purcell-Meiboom-Gill echo train (for which rotation angle errors cancel out after each cycle of two π pulses).

Unlike in Reference [5], we cannot observe the train of nuclear spin echoes as they form, because our detection requires transferring the coherence to the electron spin for detection via electron spin echo. Instead, we observe the final echo intensity following a $n = 2$ pulse or $n = 4$ pulse dynamical decoupling (DD) sequence of π pulses of phase θ with respect to the phase of the initial nuclear spin coherence. For $\theta = 0, \pi, 2\pi, ...$, this DD sequence is identical with a Carr-Purcell sequence. For $\theta = \pi/2, 3\pi/2, ...$ it is identical with a Carr-Purcell-Meiboom-Gill sequence. Thus as a function of θ, we see an oscillation in the final echo amplitude, where the ratio between the minimum and maximum signal is given by $\exp\left[-\sigma_{\mathrm{RF}}^2 n^2\right]$, where σ_{RF} is the standard deviation of the Gaussian distribution of RF B_1 fields across the sample.

We performed this procedure for the two RF transitions from the $m_I = -1/2$ state. Fitting the variation of the final echo amplitude with θ yielded an estimate of the RF pulse fidelity of $93.5 \pm 0.1\%$ for RF pulses at both frequencies.

VII. CALIBRATION OF THE ARTIFICIAL PHASE GATE

A controlled artificial phase perturbation, $\widehat{Z(\theta)}$, was applied to investigate how the logical qubit evolves under a transient fluctuation of the magnetic field (Fig. 3 in the main text). This artificial phase perturbation is achieved by the generation of a transient magnetic field that is parallel to the static B_0 field. We first calibrate the effect of $\widehat{Z(\theta)}$ by measuring its effect on a standard nuclear coherence between two states.

The calibration sequence is shown in Fig. S6(a). The spin control pulses are the same as the coherence transfer scheme described in Fig. S2(b) with a magnetic field pulse (B-field pulse) applied during the first free evolution period of the nuclear spin. Such a B-field pulse modifies the precession frequency for the nuclear spins, leading to a phase shift in

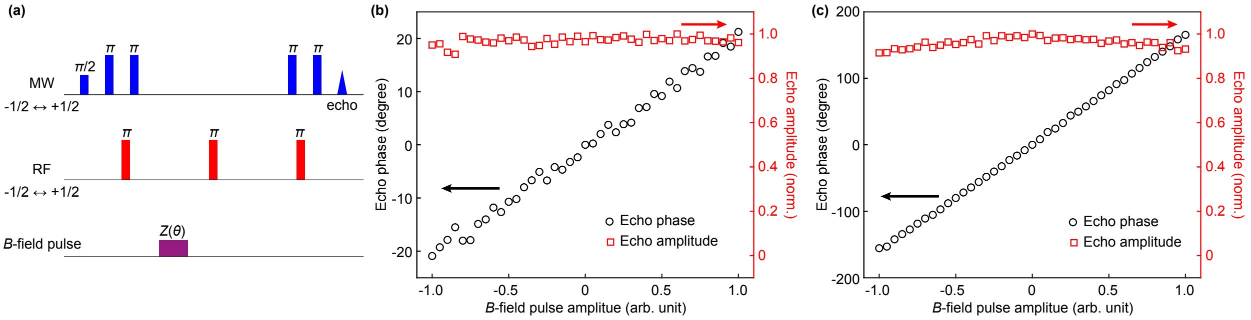

FIG. S6. **(a)** the pulse sequence for the calibration of the artificial phase perturbation $\widehat{Z(\theta)}$. The phase and the amplitude of the echo are measured while varying the amplitude of the B-field pulse with a duration of 10 μs **(b)** and 80 μs **(c)**.

the final echo. The calibration results are shown in Fig. S6(b) and (c), where the duration of the B-field pulse is fixed to 10 μs and 80 μs, respectively, while the amplitude of the pulse is varied. A linear phase dependence on the B-field pulse amplitude was observed for both pulse durations, with the effect of the 80 μs pulse approximately 8 times that of the 10 μs pulse. The results confirm that the phase shift is proportional to both the duration and the amplitude of the applied B-field pulse. Furthermore, the amplitude of the echo remains stable throughout the experiment, with a maximum 10% modulation observed for the strongest 80 μs B-field pulse. This confirms that a reasonably homogeneous B-field pulse is applied across the sample. Any inhomogeneity in the transient magnetic field pulse will reduce the echo signal by introducing a phase distribution to the spin ensemble, similar to the ones describe in Sec. VIII. However, such inhomogeneity only exists during the B-field pulse, and therefore cannot be eliminated by the refocusing pulse.

VIII. REFOCUSING THE QUDIT STATE

In the experiment described in this work we must consider the effect of inhomogeneous broadening across the spin ensemble. The effect of inhomogeneous broadening leads to some electron/nuclear spins detuned from the applied MW/RF radiations, resulting in an undesired phase distribution for the quantum coherence stored the spin ensemble. Such effects must be mitigated using carefully placed refocusing pulses to allow proper coherence transfers and echo detections.

The inhomogeneous broadening effect for the electron spins can be removed straightfor-

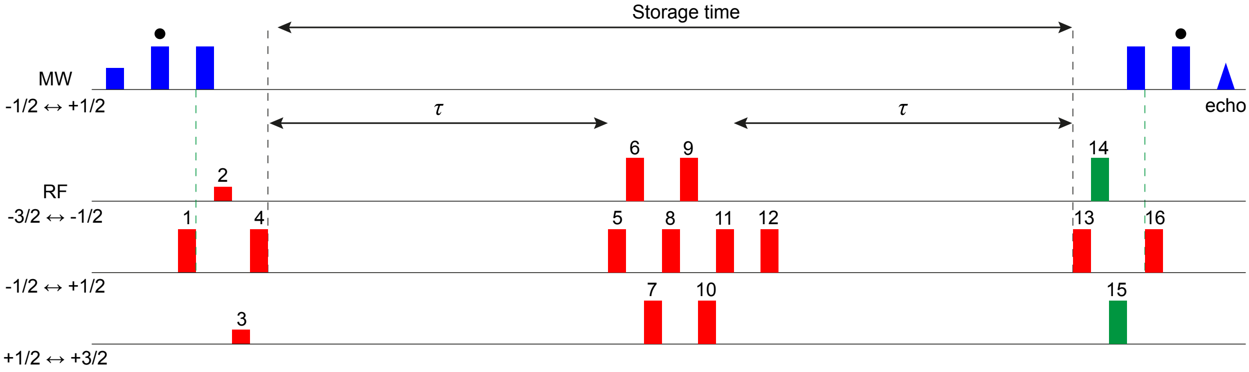

FIG. S7. The pulse sequence for quantum error correction with nuclear logical qubits. An electron spin coherence is generated by the very first MW pulse and then transferred to the hyperfine-coupled nuclear spin. The MW refocusing pulses are labeled with •. The MW pulses are aligned to the RF pulse 1 and 16 as indicated by the vertical dashed lines. All RF pulses are labeled with their information listed in Table II. The RF pulses in the dashed box serve as the refocusing operation for the nuclear logical qudit.

wardly since the coherence is stored in the superposition of two electron spin eigenstates of $|-1/2\rangle \otimes |-1/2\rangle$ and $|+1/2\rangle \otimes |-1/2\rangle$. This allows us to eliminate the inhomogeneities in the electron spins by applying the two MW π refocusing pulses in the encoding/decoding parts as shown in Fig. S7. By comparison, refocusing the nuclear qudit state is more challenging because the quantum coherence is stored in a four dimensional Hilbert space. For the quantum coherence stored in the superposition of two nuclear spins states with $\delta m_I = 1$, the inhomogeneous broadening induced phase is $\delta f_i \times \tau$, where δf_i is the detuning of the nuclear spin Larmour frequency from the RF control radiation of f_i and τ is the free evolution time of the spin. The nuclear spin transition frequencies for Mn:ZnO can be directly modulated by the nuclear Zeeman interaction, the hyperfine interaction and the nuclear quadrupole moment. The latter two couple to different transitions differently, making $\delta f_1 \neq \delta f_2 \neq \delta f_3$ and leading to three phases that cannot be eliminated using a simple refocusing pulse. Additionally, the fault tolerant memory protocol requires the coherence to be (almost) always encoded using the logical qubits, preventing us from refocusing by cycling the coherences between different superpositions periodically [6].

We design a composite refocusing sequence as shown in Fig. S7. Table II shows the exact position of all RF pulses involved in the fault tolerant memory sequence. In a practical

TABLE II. The parameters for the RF pulses used in the quantum error correction sequence.

Pulse #	1	2	3	4	5	6	7	8
Frequency	f_2	f_1	f_3	f_2	f_2	f_1	f_3	f_2
Position	0	U	$2U$	$3U$	$3U+\tau$	$4U+\tau$	$5U+\tau$	$6U+\tau$
Ampl. & phase	$+\pi$	$+\pi/3$	$+\pi/3$	$-\pi$	$+\pi$	$\pm\pi$	$+\pi$	$+\pi$

Pulse #	9	10	11	12	13	14	15	16
Frequency	f_1	f_3	f_2	f_2	f_2	f_1	f_3	f_2
Position	$7U+\tau$	$8U+\tau$	$9U+\tau$	15U + τ	$9U+2\tau$	$10U+2\tau$	$11U+2\tau$	$12U+2\tau$
Ampl. & phase	$\pm\pi$	$\pm\pi$	$-\pi$	$+\pi$	$+\pi$	$+\pi$	$+\pi$	$+\pi$

experiment, one needs to take into account the finite duration of the RF pulses and the ring down behaviour of the RF coil. To compensate for these effects, we introduce small delays between consecutive RF pulses, multiples of U $(= 8\ \mu\text{s} \ll \tau)$, as listed in Table II. For QEC experiemnt with artificial error (Fig.2 in main text), τ was fixed to 0.1 ms, and for experiment with varying storage time (Fig.3 in main text), τ was changed from 0.1 ms to 3 ms. Pulses 5 to 12 act effectively as a π pulse over the four dimensional nuclear spin subspace of $m_I = -3/2, -1/2, +1/2$ and $+3/2$. Note pulses 6, 9 and 10 are alternated between $+\pi$ and $-\pi$ pulses in experiments. This alternation, together with varying the phase of the first MW coherence generation pulse, produces a four step phase cycling that reduces undesired echo contributions, similar to that described in Table I. The refocusing block can be represented by the propagator

$$\mathbf{P}_{\text{refocus},\pm} = \begin{pmatrix} 0 & 0 & 0 & \pm 1 \\ 0 & 0 & \pm 1 & 0 \\ 0 & +1 & 0 & 0 \\ +1 & 0 & 0 & 0 \end{pmatrix} \tag{S21}$$

where the + and − sign in the subscript corresponds to pulses 6, 9 and 10 being $+\pi$ or $-\pi$, respectively. Here we only present the nuclear spin part for clarity since the electron spin is always in the $m_S = -1/2$ state when the coherence is stored in the nuclear spin.

An arbitrary nuclear superpostion state, $|-1/2\rangle \otimes |\psi\rangle$ with $|\psi\rangle$ being the nuclear spin part, undergoes a period τ of free evolution where the effect of inhomogeneous broadening has the effect:

$$|\psi\rangle = \begin{pmatrix} \xi \\ \zeta \\ \eta \\ \lambda \end{pmatrix} \xrightarrow{\text{time } \tau} |\psi(\tau)\rangle = \begin{pmatrix} \xi e^{-\mathrm{i}(\delta f_1+\delta f_2+\delta f_3)\tau} \\ \zeta e^{-\mathrm{i}(\delta f_1+\delta f_2)\tau} \\ \eta e^{-\mathrm{i}\delta f_1 \tau} \\ \lambda \end{pmatrix} \tag{S22}$$

$|\psi(\tau)\rangle$ is the state before the refocusing pulses are applied (immediate before pulse 5) up to an unimportant global phase. Note this effect is different from the artificial perturbation shown in the main text in that (1) different m_I coherence gain a different phases and (2) the same effect will persist throughout the entire pulse sequence. The refocussing pulses then swap the coherence within the subspace, allowing the nuclear spins to evolve for another period of τ under the same inhomogeneous shifts, as

$$\mathbf{P}_{\text{refocus},\pm}|\psi(\tau)\rangle = \begin{pmatrix} \pm\lambda \\ \pm\eta e^{-\mathrm{i}\delta f_1 \tau} \\ \zeta e^{-\mathrm{i}(\delta f_1+\delta f_2)\tau} \\ \xi e^{-\mathrm{i}(\delta f_1+\delta f_2+\delta f_3)\tau} \end{pmatrix} \xrightarrow{\text{time } \tau} |\psi(2\tau)\rangle = \begin{pmatrix} \pm\lambda e^{-\mathrm{i}(\delta f_1+\delta f_2+\delta f_3)\tau} \\ \pm\eta e^{-\mathrm{i}(2\delta f_1+\delta f_2)\tau} \\ \zeta e^{-\mathrm{i}(2\delta f_1+\delta f_2)\tau} \\ \xi e^{-\mathrm{i}(\delta f_1+\delta f_2+\delta f_3)\tau} \end{pmatrix}, \tag{S23}$$

where $|\psi(2\tau)\rangle$ is the state ready to be decoded and transferred back to the electron spin for the read-out process.

When the initial state is an encoded logical qubit defined by Eqn. 3 of the main manuscript, this refocusing sequence retains the quantum information using logical qubits throughout the storage time of 2τ. Eqn. S23 shows that the coherence stored in the superpositions $|-1/2\rangle \otimes |-3/2\rangle \leftrightarrow |-1/2\rangle \otimes |+3/2\rangle$ and $|-1/2\rangle \otimes |-1/2\rangle \leftrightarrow |-1/2\rangle \otimes |+1/2\rangle$ are refocussed for any type of inhomogeneity. The other coherences, those in the superpositions $|-1/2\rangle \otimes |-3/2\rangle \leftrightarrow |-1/2\rangle \otimes |-1/2\rangle$ and $|-1/2\rangle \otimes |+3/2\rangle \leftrightarrow |-1/2\rangle \otimes |+1/2\rangle$ cannot be refocussed using our sequence. Nevertheless, the two recovered coherences allow us to extrapolate the information about the evolution of the encoded state using the measurement scheme described in the main text.

IX. OVERLAP OF LOGICAL QUBIT AND ERROR COMPONENT WITH ARTIFICIAL ERROR

In Fig. S8, we present the overlap of logical qubit ($\langle\psi_L|\widehat{Z(\theta)}|\psi_L\rangle$) and the error component ($\langle\psi_L|\hat{I}_z^{\dagger}\widehat{Z(\theta)}|\psi_L\rangle$) obtained (1) by theoretical calculation (dashed lines) and (2) from the

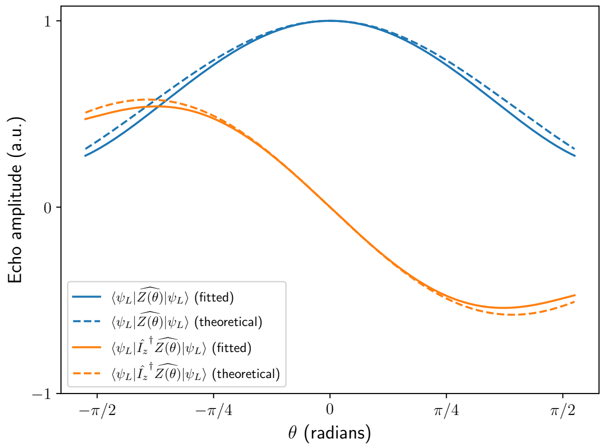

FIG. S8. Solid lines: Estimates of the quantities $\langle\psi_L|\widehat{Z(\theta)}|\psi_L\rangle$ and $\langle\psi_L|\hat{I}_z{}^\dagger\widehat{Z(\theta)}|\psi_L\rangle$ extracted from the parameterised fit to the experimental data. Dashed lines: exact theroetical evolution of the same quantities.

fitting of experimental data (solid lines), as a function of the artificial error θ that we applied. The measured part is constructed from the parameters A_n, $n = 0\cdots5$. As expected for small θ, $\langle\psi_L|\widehat{Z(\theta)}|\psi_L\rangle$ is independent of θ and $\langle\psi_L|\hat{I}_z{}^\dagger\widehat{Z(\theta)}|\psi_L\rangle$ varies linearly with θ.

This demonstrates the general point that using the parameterisation, we can explore the evolution of physically meaningful quantities that we cannot measure directly.

X. EXPERIMENTAL SETUP

Our custom-built spectrometer is sketched in Fig. S9. The important feature of the setup is that all time-dependent control signals are sourced from a single arbitrary waveform generator. This includes all microwave (MW) electron spin resonance pulses and radio frequency (RF) nuclear spin resonance pulses. This facilitates the implementation of the complex multifrequency coherent sequences required for this experiment.

The parts assigned with numbers are:

(1) Clock, 10MHz TTL-reference: Stanford Research Systems FS725
(2) Arbitrary waveform generator (AWG): Zurich instruments, HDAWG 750 MHz, 4 ports
(3) Microwave (MW) source: Keysight EE8257D PSG Signal Generator
(4) IQ-mixer for up-conversion: MLIQ-0416, 4-16 GHz
(5) Amplifier for MW-pulses: ERZIA ERZ-HPA-0850-0980-55, 8.5-9.8 GHz, 300 W

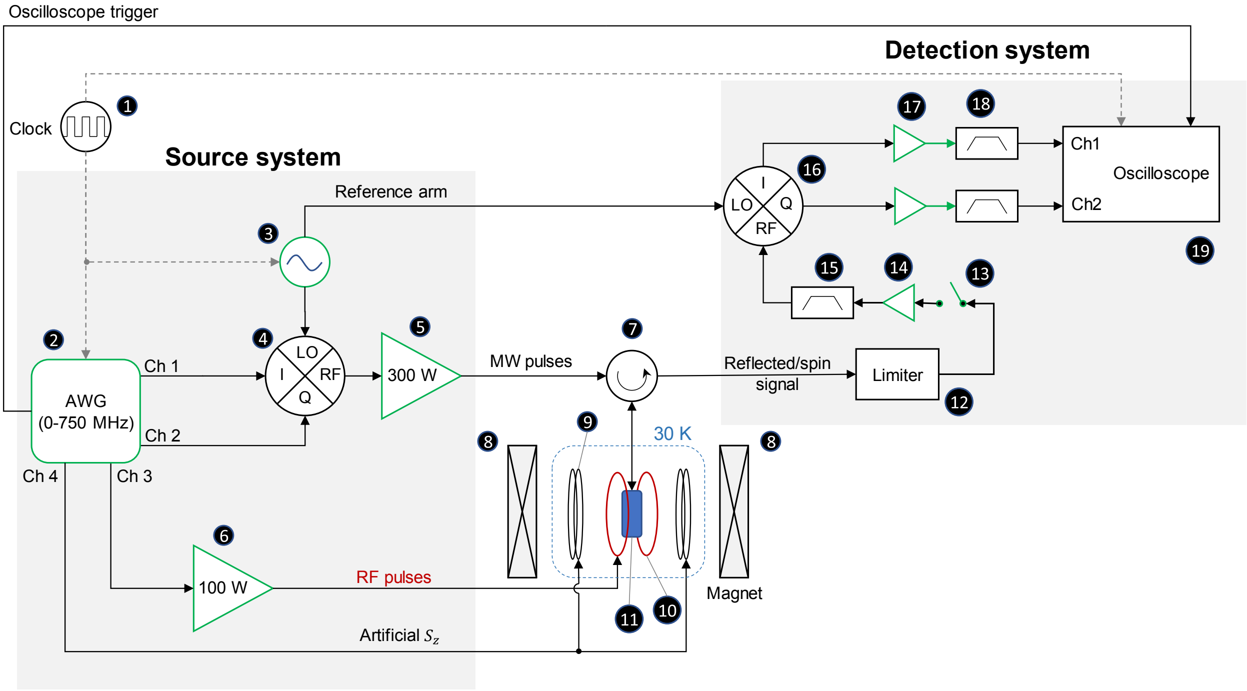

FIG. S9. Schematic diagram of experimental setup in this work.

(6) Amplifier for RF-pulses: Mini-Circuits ZHL-100W-52-S+, 50-500 MHz, 100 W

(7) Microwave X-band circulator

(8) Resistive magnet: 0 - 0.97 T

(9-11): Bruker EN 4118X-MD4 resonator combined with an Oxford Instruments cryostat

(9) Modulation coils

(10) RF ENDOR coils

(11) MW cavity, sample location

(12) Limiter: Narda LIM 201, 1-18 GHz, max 1 μs at 150W

(13) Protection switch: SP213DHTS-80, 70 dB isolation

(14) Cascade of low-noise MW amplifiers: Narda-MITEQ LNA-40-08001200-09-10P, and Mini-Circuits ZX60-05113LN+

(15) Cavity bandpass filter: Mini-Circuits ZVBP-9750-S+, 9.5-10 GHz

(16) IQ-mixer for down-conversion: MLIQ-0416, 4-16 GHz

(17) Preamplifier: Stanford Research Systems SR445A, 350 MHz, 13dBm

(18) Bandpass filter: Mini-Circuits BBP-100+, 87-117 MHz

(19) Oscilloscope: Tektronix DPO7254

During measurements, the sample is located in the microwave (MW) cavity of the Bruker MD4 resonator (11), the static magnetic field B_0 is generated by the resistive magnet (8), and the reference 10 MHz-signal is provided by the frequency standard (1).

Pulse sequences are programmed in Python on an external computer and are uploaded onto the AWG (2). The shot repetition time is determined by the longitudinal nuclear spin relaxation time T_{1n} (which limits the thermalisation time) of the system under study and is encoded as a wait period in the pulse-sequence code.

The external computer triggers the AWG (2) making it produce a required number of identical pulse-sequences (shots). At the end of each sequence, the AWG (2) sends a TTL trigger signal to the oscilloscope (19). The TTL pulse is synchronised with the RF and MW pulses.

RF pulses are generated by the AWG (2) and get directly multiplied at (6) before they are fed to the RF coil of the Bruker MD4 resonator (10). As for MW pulses, the AWG (2) first generates the envelopes of MW pulses at 100MHz and sends them to the IQ-mixer (4), where they get mixed with the 9.6 GHz signal from the MW-source (3) and undergo up-conversion to about 9.7 GHz. After that, the MW pulses get amplified at (5) and enter the MW cavity of the MD4 resonator (11) directed by the circulator (7). A proper alignment of the MD4 resonator allows one to ensure that MW-field B_1, RF-field B_2 and the static field B_0 are mutually perpendicular.

The excitation MW pulses reflected from the resonator cavity and the useful echo signals generated by the spin system are directed by the circulator (7) towards the detection circuit of the spectrometer. The excitation pulses are prevented from entering and damaging the detection system by the limiter (12) and protection switch (13). The opening time of the switch defines the dead-time of the spectrometer. After the switch is closed, the signal produced by the spin system can proceed to the cascade of low-noise amplifiers (14), band-pass filter (15), and to the IQ-mixer (16) where it gets down-converted to 100 MHz using the reference arm from the MW-source (3). The use of the IQ-mixer (16) allows us to perform quadrature detection and obtain both the in-phase and quadrature components of the signal. Both down-converted signals get amplified at (17), pass the band-pass filters (18), and reach the oscilloscope (19). The echoes resulting from separate shots of identical pulse-sequences are accumulated by the oscilloscope (19). Finally, the external computer downloads the averaged signal from the oscilloscope for further data processing.

The artificial B_z fluctuation was implemented using the modulation coils of the MD-4 resonator (9). The corresponding pulses were incorporated into the pulse sequences uploaded to the AWG (2), whose output was fed to the modulation coils (9).

[1] R. E. George, J. P. Edwards, and A. Ardavan, Coherent spin control by electrical manipulation of the magnetic anisotropy, Phys. Rev. Lett. **110**, 027601 (2013).

[2] S. Asaad, V. Mourik, B. Joecker, M. A. I. Johnson, A. D. Baczewski, H. R. Firgau, M. T. Madzik, V. Schmitt, J. J. Pla, F. E. Hudson, K. M. Itoh, J. C. McCallum, A. S. Dzurak, A. Laucht, and A. Morello, Coherent electrical control of a single high-spin nucleus in silicon, Nature **579**, 205 (2020).

[3] J. J. L. Morton, A. M. Tyryshkin, R. M. Brown, S. Shankar, B. W. Lovett, A. Ardavan, T. Schenkel, E. E. Haller, J. W. Ager, and S. A. Lyon, Solid-state quantum memory using the 31P nuclear spin, Nature **455**, 1085 (2008).

[4] E. Knill, I. Chuang, and R. Laflamme, Effective pure states for bulk quantum computation, Physical Review A **57**, 3348 (1998).

[5] J. J. L. Morton, A. M. Tyryshkin, A. Ardavan, K. Porfyrakis, S. A. Lyon, and G. A. D. Briggs, Measuring errors in single-qubit rotations by pulsed electron paramagnetic resonance, Physical Review A **71**, 012332 (2005).

[6] N. V. Vitanov, Dynamical rephasing of ensembles of qudits, Physical Review A **92**, 022314 (2015).